Available online at www.sciencedirect.com
SCIENCE DIRECT
ELSEVIER
Journal of the European Ceramic Society 26 (2006) 2653–2667
ECERS
www.elsevier.com/locate/jeurceramsoc

Effect of particle shape and arrangement on thermoelastic properties of porous ceramics

F. Raether *, M. Iuga

Fraunhofer Institut Silicatforschung, Würzburg, Germany

Received 30 March 2005; received in revised form 6 July 2005; accepted 16 July 2005
Available online 26 September 2005

Abstract

Thermoelastic properties of various bi-continuous porous ceramics are simulated by a new finite element model. The model considers various particle shapes which allow for an independent variation of pore volume and particle contact area. Phenomena like neck formation, agglomeration, particle size distribution and coordination are included in the model geometry. Particle arrangement is modelled using cubic super cells as well as random particle positions. Young's moduli, Poisson's ratios and stress concentration factors are simulated and thermal shock resistance is estimated from these data. A close correlation between thermal conductivity and Young's modulus is found for all types of microstructure. Stress concentration is strongly affected by the particle shapes in the contact region.

Keywords: Thermal properties; Thermal conductivity; Mechanical properties; Strength; Porosity

1. Introduction

Sintering of any ceramic starts with a green compact with convex weakly bonded particles and open pores. It forms sintering necks, pore channels and finally closed pores at high temperatures. The interpretation and prediction of sintering behaviour, e.g. the distribution of thermal stress, require the knowledge of thermoelastic properties in all stages of sintering. Vice versa, the knowledge of thermoelastic properties allows an insight into microstructure development during sintering if a sufficiently unique relation between microstructure and macroscopic properties can be established. Moreover, porous ceramics are widely used as filters, membranes and as thermal isolators or as a matrix phase in oxidic ceramic matrix composites (OCMC). For many applications, e.g. high thermal shock resistance, specific thermoelastic properties are required. A future design of those materials will rely on an accurate simulation of material properties from microstructures features.

Some thermoelastic properties in porous compacts are simply determined by a rule of mixtures or by the respective property of the solid phase, e.g. density, heat capacity and coefficient of thermal expansion.[1] On the other hand, thermal conductivity and elastic coefficients are strongly related to microstructure. Whereas in isotropic materials thermal conductivity is determined by a single number, elastic behaviour is described by two of a set of four properties: Young's modulus, Poisson's ratio, bulk modulus and shear modulus. In the present paper Young's modulus and Poisson's ratio were used. (Bulk and shear modulus can be easily derived from the former two.[2]) The consideration of strength is more difficult, since it is usually limited by flaws, which are not included in most microstructure simulations. However, the stress concentration within the microstructure was calculated in the present study.

Previous studies have concentrated on the investigation of the relation between total pore volume and thermoelastic properties of porous compacts.[1,3–14] Polynomial equations have been derived heuristically. They were applied to a large amount of experimental data[8,11] which however demonstrates the large uncertainty in the experimental data rather than any theoretical justification of the polynomials. Varia-

* Corresponding author.
E-mail address: raether@isc.fraunhofer.de (F. Raether).

0955-2219/$ – see front matter © 2005 Elsevier Ltd. All rights reserved.
doi:10.1016/j.jeurceramsoc.2005.07.059

tional principles have been used to obtain rigorous upper and lower bounds for the properties of composites with given properties of the participating phases.[4,15] However, the thermoelastic properties of pore phase and solid phase in porous compacts differ by at least three orders of magnitude, resulting in a large gap between lower and upper bounds. For decades effective media theories have been developed as well.[3,12,16–20] Using effective media theories one can sufficiently describe microstructures with closed pores. If the pore fraction is small, the composite properties can be calculated with high accuracy for ellipsoidal pores.[21] On the other hand, for bi-continuous materials like porous compacts with open pores, microstructure can only be considered through the volume fractions of phases.[21] A more specific description of microstructure was provided by the minimum solid area approach.[22,23] The minimum area of solid phase perpendicular to the heat flux or applied force was used to estimate the respective composite property. The advantage of the minimum solid area approach is its simplicity and its applicability to all kinds of microstructures. However, it will be shown below that its predictions are not very accurate for many bi-continuous microstructures.

Increasing computer power favours the simulation of specific microstructures. Heat flow has been simulated using random walk[24,25] and finite difference methods,[26] but today finite element based methods get more attention since they are easily available and can be used for the calculation of thermal as well as mechanical properties.[6,13,27–38] Although 2-D models are still used, many topological features, e.g. particle connectivity, cannot be adequately described in two dimensions and generally 3-D models are to be preferred. There are two types of 3-D models: periodic lattices and random structures. The periodic lattices are calculated with spherical particles or pores in a simple cubic (sc), body centred cubic (bcc) or face centred cubic (fcc) arrangement.[6] Sintering necks are simulated using truncated spheres[6] or sometimes overlapping cylinders.[39] Random microstructures are produced in different ways. Often ellipsoidal particles or pores with randomly chosen centres and more or less overlap are generated.[6,37] Those random structures look much more similar to real microstructures. The disadvantage of both types of geometric models is that fundamental phenomena like sintering neck growth and its effect on thermoelastic properties, cannot be described using simple particle shapes. It was shown experimentally that neck growth caused by surface diffusion increases thermal conductivity[40] and Young's modulus[41] dramatically without a change in porosity. Another important phenomenon that needs better theoretical insight is agglomeration. Particle clusters forming dense regions interconnected by less dense porous regions have been related to experimentally observed smaller elastic moduli compared to homogeneous materials.[42] Anyhow, the effect of agglomeration on thermoelastic properties has not been simulated so far.

The purpose of the present paper is to introduce particle shapes and arrangements, which allow for a simulation of the effect of contact area, agglomeration and particle size on thermoelastic properties. Using simplified microstructures we aim at a better understanding of principal effects. The evolution of microstructure is not simulated.

2. The finite element model

2.1. Particle shapes

Different solid particles have been used in the simulations. Fig. 1 shows some elementary particle shapes within their simple cubic unit cell. Truncated spheres (Fig. 1a) were valuable in more complex particle arrangements (see below). The truncated octahedron (Fig. 1b) was used to compare the effect of curved particle surfaces to flat surfaces as the latter can occur during sintering of crystalline particles with anisotropic surface energy. The overlapping spheres and cylinders (Fig. 1c) were considered since overlapping cylinders were introduced by other authors.[35,39] The sphere at the centre of the cell has been added to be able to vary the radius r of the cylinders—which is identical to the particle contact radius—independently from the solid volume fraction. (For the overlapping cylinders as well as for the truncated sphere and octahedron the structure is completely described by the solid volume fraction.)

A solid volume fraction of 70% has been used in Figs. 1–8. It was calculated from the radii and edge lengths of the respective simple bodies using elementary geometry. The inverse problem of finding the radii and edge lengths for given volume fractions has been solved numerically using in-house software.

Fig. 2 shows a particle type, which allows a much larger variation of neck area than the overlapping sphere and cylinders. It is formed by a cube (edge length b), which has 6 or 24 cylindrical contacts (with radius r) to its 6 neighbours. Although this particle type looks somewhat artificial, similar to a Lego brick, it was considered helpful in understanding microstructures in intermediate stage sintering. Those structures are frequently formed by dense agglomerates loosely connected by small elongated particles. Fig. 3 shows a structure, which is very flexible too, but looks more similar to an individual powder particle. It is formed by six truncated square pyramids based on the sides of an enclosed cube. The lateral surfaces of the pyramids meet at a constant opening angle (similar to the dihedral angle) at the edges of the particle contacts. The structure is completely determined by this opening angle Θ and the volume fraction of solid phase f_s:

$$f_s = \frac{a^3 + 8\,h^2 b + 8\,h\,b^2 - 12\,abh}{a^3};$$

$$h = b[1 + \tan\,(\Theta)^{-1}]^{-1}; \quad (1)$$

with b = edge length at contact area of pyramids (particle contact area = b^2); h = height of pyramids; and a = edge length of unit cell. Increasing the opening angle at constant volume fraction causes a drastic increase of the contact area (Fig. 3).

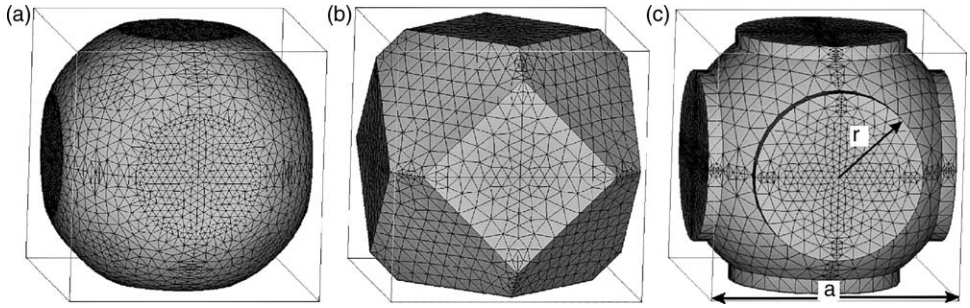

Fig. 1. Simple cubic particles used in the FE simulations: (a) truncated sphere, (b) truncated octahedron, and (c) overlapping sphere and cylinders. Grey lines indicate the unit cell.

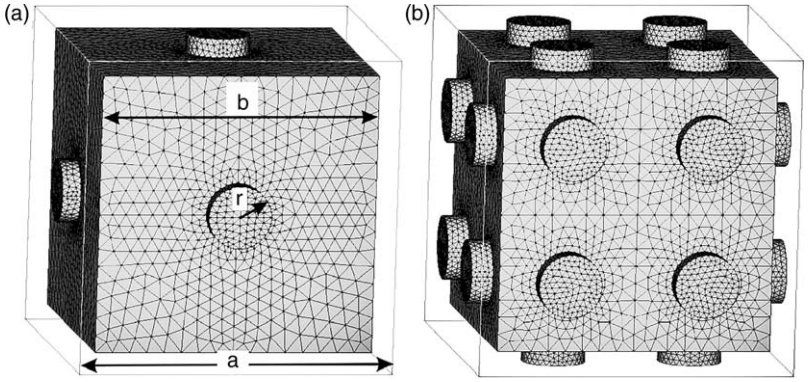

Fig. 2. Extreme particle shapes used to describe microstructures with high solid volume fractions and small sintering neck areas: (a) cube with 6 cylindrical contacts, and (b) cube with 24 cylindrical contacts.

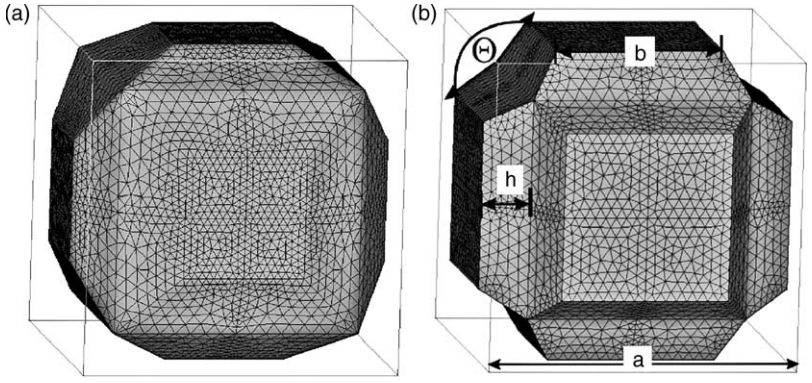

Fig. 3. Particles formed by six truncated square pyramids based on the sides of an enclosed cube with different opening angles Θ: (a) $\Theta = 60^\circ$, and (b) $\Theta = 120^\circ$.

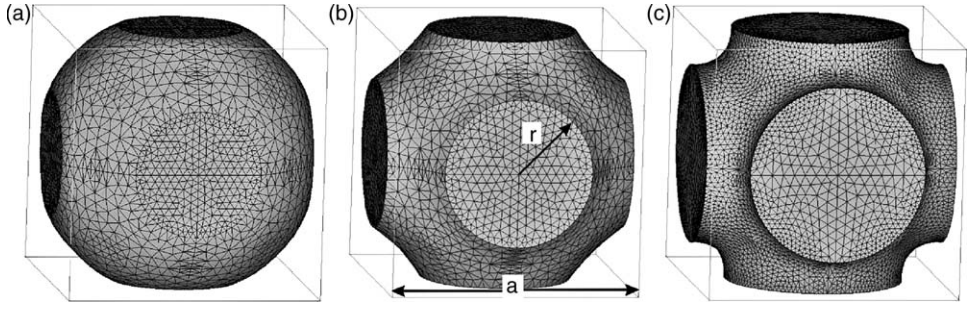

Fig. 4. Particles formed by minimising the interface energy at given ratio between neck radii r and edge length of unit cell a: (a) $r/a = 0.5$, (b) $r/a = 0.6$, and (c) $r/a = 0.7$.

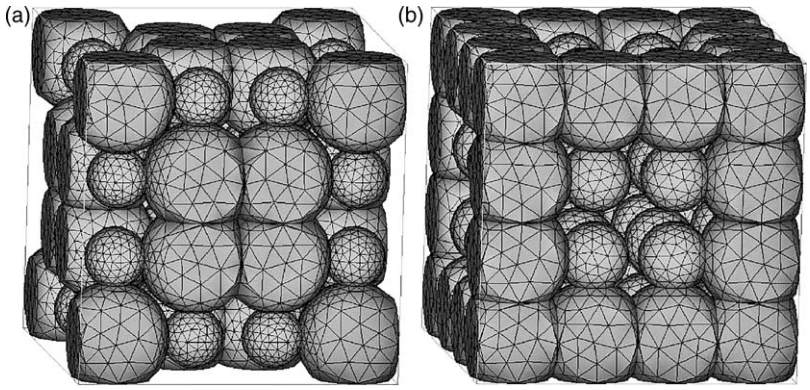

Fig. 5. Cubic microstructure with (a) homogeneous and (b) inhomogeneous arrangement of small and large spherical particles.

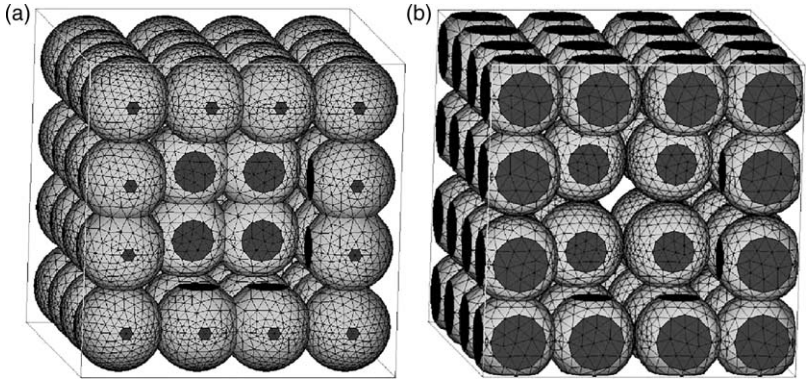

Fig. 6. Cubic microstructure with spherical particles shifted towards (a) the centre and (b) the sides of the unit cell. Some particles were removed to get a better view of the microstructure.

Since the plane faces of the structure with truncated square pyramids only reflect materials with anisotropic interface energy another microstructure has been generated by looking for the particle pore interface with minimum energy—assuming that the interface energy does not vary with crystal direction (Fig. 4). A similar approach was at first described by Beere.[60] For given volume fractions of the two phases and given spherical neck areas (with neck radius r), the minimisation was performed by the computer program Surface Evolver.[43] It was started with a simple prescribed geometry of cubic symmetry and with correct volume fractions. (Due to the high symmetry of the cubic structure only 1/48th of the volume of the unit cell was actually minimised and the structures shown in Fig. 4 were constructed by symmetry operations.) The interface was composed of small plane triangular facets defined by the coordinates of their vertices. The vertices were moved after subsequent iterations according to an individual force vector. The force vector was calculated locally for each vertex from the tensile stresses originating from the neighbouring vertices. Appropriate constraints were

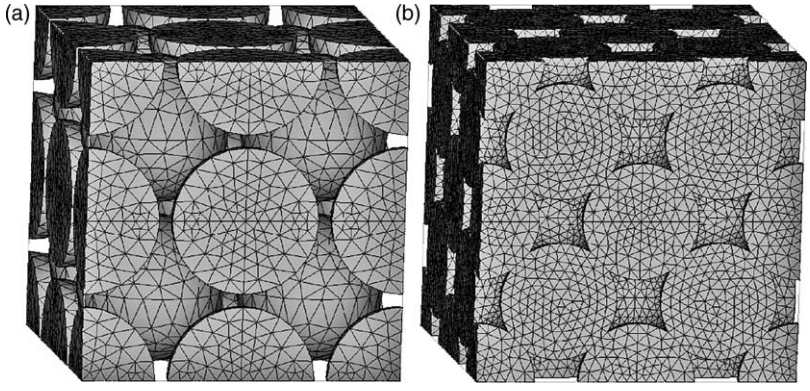

Fig. 7. Cubic microstructure with spherical particles: (a) 8 and (b) 12 nearest neighbours (bcc and fcc structures, respectively).

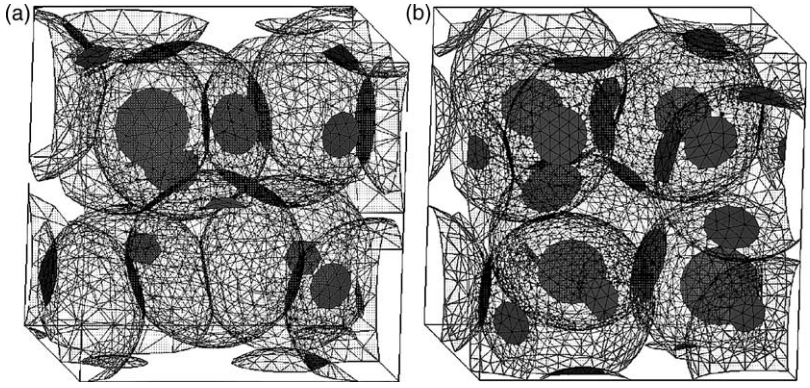

Fig. 8. Random structure of spherical particles with periodic boundaries and the ratio between total contact area and total pore–solid interface area of 0.1; on average having (a) 4.75 contacts per particle and (b) 7.5 contacts per particle. Here the solid particles are transparent and the contact areas are represented with the grey colour.

used to ensure that the cubic symmetry was maintained during the minimisation. The mesh was successively refined ending up with about 100–200 vertices. Convergence was achieved after a total of about 100 iterations. Computational time was less then 1 min on a usual PC. From Fig. 4 it can be seen that curvature at the interface changed from convex to concave if the sintering neck radius, r was increased.

2.2. Particle arrangement

Between the simple cubic structures described in the previous paragraph and random structures described below, an intermediate step was introduced. Super cells of cubic symmetry with some tens of particles have been used to study the effect of particle size, displacement and co-ordination. Taking care of the requirement to maintain the cubic symmetry the allowed geometrical variations are reduced. From all the particles shown in the previous section only truncated spheres have been used for the simulations of super cells and random structures, because spherical geometry can be applied most conveniently in more complex particle arrangements.

The effect of particle size was studied using a bimodal distribution with two different sphere diameters. Particle arrangement was either homogeneous, i.e. smaller particles were surrounded by larger particles and vice versa, or inhomogeneous, i.e. the smaller particles were in the centre of the super cell and the larger particles at the edges. Fig. 5 shows two different unit cells with 64 particles—each having 6 nearest neighbours—and homogeneous or inhomogeneous particle arrangement, respectively. The homogeneous and inhomogeneous arrangement should reflect different attractive and repulsive forces between the smaller and larger particles during the forming process. (To reduce the number of parameters in the simulations, the number fraction of larger and smaller particles was always 50% and their thermoelastic properties were equated.)

Particle displacements were introduced to simulate agglomeration or the formation of large pores during sintering. Considering cubic symmetry, a simple transformation was used which generates a constant gradient in mass. For that the centres of the particles were shifted by a displacement vector whose ith component u_i was calculated according to:

$$u_i = \frac{r_i - c_i + a}{2}(c_i - r_i)\frac{d_{\text{shift}}}{a}; \tag{2}$$

with r_i = component i of initial centre position of particle, c_i = component i of centre of unit cell, a = edge length of unit cell, d_{shift} = dimensionless parameter, which controls the amount of the displacement.

Parallel to the coordinate axes, the displacement was largest at a distance of $a/4$ from the centre where it amounted to $ad_{\text{shift}}/16$. If d_{shift} was positive, the particles were shifted towards the centre and if it was negative, the particles were shifted towards the sides of the unit cell which corresponded to agglomeration and pore formation, respectively (Fig. 6).

Besides the structures with 6 nearest neighbours shown in the previous section, structures derived from bcc and fcc lattices with 8 and 12 nearest neighbours have also been used (Fig. 7). Therefore, the number of nearest neighbours used in the simulations covered the range of nearest neighbours observed in green compacts (6–8) and sintered materials (12–14).[44] Considering the restrictions described in the previous paragraphs, particle size, displacement and number of nearest neighbours could be varied at the same time without violating the cubic symmetry of the super cell.

Random structures were derived from a Poisson distribution of sphere centres within a cube. Initial centre positions were obtained by a standard random number generator. Typically, four to eight initial spheres were used for one microstructure. Particle compaction was considered by starting with a large unit cell and subsequently reducing its size by an affine transformation of the particle centres. The centres of contacting spheres were shifted by an individual displacement vector for each sphere, which was calculated from all its contacts, to prevent overlap with neighbouring spheres. When density was high enough, the movement of the spheres was restricted by other contacts. Then overlapping of spheres was allowed and the total elastic energy of all spheres within

the unit cell was minimised by applying a common scaling factor to the individual displacement vectors. The scaling factor was always between 0 (soft sphere limit) and 1 (hard sphere limit). Elastic energy was determined from the sum of the local energies determined by contact area and sphere radii.[45] According to Gusev et al.[32] periodic boundaries were introduced by shifting those parts of spheres, which lay outside the cube to the respective opposite sides of the cube (Fig. 8). This increased the total number of spheres 14–21. After the random structures had been determined, their validity was carefully checked. The criteria are explained in the next paragraph. Since many structures had to be generated to find one valid structure the computational effort for generating the random structures was much higher than for the cubic super cells. The random structures were produced by an in-house software running overnight. It enabled the generation of random structures with additional specified geometric properties, e.g. a fixed average number of contacts per particle, by automatically generating and testing thousands of structures until the required properties were met (Fig. 8a and b).

Sintering necks were constructed as planes defined by the circular edge of the overlap region of two spheres. To avoid conflicts in the construction of sintering necks only those arrangements were chosen for the FE simulations, which did not have any region where more than two particles overlapped. For the same reason structures were disregarded which had any sphere centre lying within another sphere. Both constraints severely limited the possible range of parameters: e.g., for a cubic super cell with six nearest neighbours and a solid volume fraction of 70% the maximum allowable parameter d_{shift} was 24% which leads to a maximum displacement of 2.6% of the length of the unit cell. But the restrictions were considered useful since the unique definition of sintering necks was important for the interpretation of the results.

Some geometric data were derived from the microstructure. Most important were the interface area between solid and pore phase and the neck area at the particle contacts. Also the minimum solid area perpendicular to the flux or force direction was derived (according to the minimum solid area approach[22]). Finally, a chord length analysis was performed by randomly selecting the starting point and direction of 10,000 test lines within the microstructure and determining the solid and pore fractions, the number of interfaces and the mean value of the squared solid chord lengths. The solid and pore fractions and the number of interfaces from chord length analysis were used to control the microstructure (the agreement to the respective values determined exactly was within 1%). The mean value of the squared solid chord lengths c_{s^2} was used as a measure for the length of force transmission:

$$c_{s^2} = \frac{\sum_i c_i^2}{\sum_i c_i}; \tag{3}$$

with c_i = chord length of individual particles.

(The arithmetic sum of the chord lengths would simply yield the volume fraction of solid phase,[46] therefore the square was introduced to get a larger weight of the longer chords.)

The homogeneity of the microstructure was measured by an auto-correlation parameter c_a, which was calculated by summing up the products of the chord lengths of neighbouring particles:

$$c_a = \frac{\sum_i c_i c_{i-1}}{\sum_i c_i^2}. \tag{4}$$

2.3. FE mesh and boundary conditions

The software package ANSYS® (ANSYS Inc, version 8.1) and a PC work station (Intel Pentium 4 Xeon 2.8 GHz) were used for the FE simulations. Utilising the symmetry of the cubic unit cells only 1/8th of the cell volume was actually simulated, whereas for the random structures the complete cell had to be considered. The microstructures were constructed from simple 3-D geometric entities like cubes or spheres and appropriate Boolean operations, reflections and rotations. (With microstructures generated by the program Surface Evolver the nodes were directly imported into ANSYS and used as nodes for the thermal and mechanical simulations.)

Meshing was performed after generating at first a 2-D mesh at the interfaces between solid and pore phase, at the neck areas and the sides of the unit cell with a fixed number of nodes (typically 6–10) at the line segments within the microstructure. This ensured that finer regions, e.g. the contact region at small sintering necks, were meshed with a sufficiently large number of elements. (To reduce computation time the number of nodes at very small line segments was somewhat reduced.) Depending on its complexity 20,000–80,000 elements have been used to describe one microstructure. Solid and pore volume were meshed with the elements SOLID87 and SOLID187 for thermal and mechanical simulations, respectively. The material properties (thermal conductivity and Young's modulus) of the pore phase were chosen six orders of magnitude smaller than the respective properties of the solid phase. Poisson's ratios of solid and pore phase were always set to 0.25. (The results of the present paper would have been unchanged by simply not meshing the pore phase but the same FE model was also used for the simulations of composites with two solid phases.)

With cubic structures, thermal simulations have been performed by setting two opposite sides of the unit cell to different fixed temperatures and applying adiabatic boundary conditions to the remaining four sides. Thermal conductivity λ was calculated from the heat flux W (averaged at one side with fixed temperature) by:

$$\lambda = \frac{W}{a\,\Delta T} \tag{5}$$

with ΔT = temperature difference at opposite sides of unit cell.

The elastic properties in structures of cubic symmetry were determined by applying a uniaxial tensile strain. Two opposing sides of the unit cell were strained by a fixed small amount ε whereas a constraint on the other sides ensured that they remained plane during the simulation. From the resulting stress σ at one of the two strained sides the "single crystal" Young's modulus E and from the resulting strain at the perpendicular sides $\varepsilon_\perp$ the "single crystal" Poisson's ratio ν were calculated by:

$$E = \frac{\sigma}{\varepsilon};\quad \nu = \frac{\varepsilon_\perp}{\varepsilon};\quad G = \frac{\sigma_s}{\varepsilon_s}. \tag{6}$$

Different from thermal conductivity the elastic properties of cubic structures are not isotropic and therefore a second simulation was required. It was performed by applying a simple shear strain ε_s and calculating the shear modulus G from the resulting shear stresses σ_s according to Eq. (6). The procedure for non-cubic symmetry is described below. Always linear elastic behaviour was considered.

The stress concentration factor f_σ was calculated from the ratio of the maximum principal tensile stress $\sigma_{1_{max}}$ within the unit cell to the applied tensile stress σ:

$$f_\sigma = \frac{\sigma_{1_{max}}}{\sigma}. \tag{7}$$

(Since stresses were largest at the edges of the particle contacts, the stress concentration factor actually was determined by averaging the 1st principal stress at all nodes at the edge of individual contacts and selecting the maximum of these averaged values.)

The FE solution was obtained by searching the minimum of the quadratic functional of the system using a conjugate gradient method, i.e. the solutions for the degrees of freedom (d.f.) were calculated by iterating the system equations to convergence, starting with an assumed zero value for all d.f.s and following orthogonal residual vectors. Computing time was about 5 min for one direction of applied strain or thermal gradient.

For the random microstructures loads were applied in different directions. For heat flow the six independent elements λ_{ij} (with $i \le j$, $j \le 3$) of the symmetric thermal conductivity tensor K were determined by applying temperature gradients parallel to the edges of the unit cell. For stress simulations both tensile and shear strains were applied in different directions to determine the 21 independent elements c_{ij} (with $i \le j$, $j \le 6$) of the symmetric stiffness matrix C:

$$\sigma = C\varepsilon;\quad q = K\,\nabla T; \tag{8}$$

with σ = stress vector, ε = strain vector, q = heat flux vector, ∇T = temperature gradient. Stresses, strains, heat flow and temperature gradients were determined from the FE solution by calculating the weighted average over all elements within the unit cube:

$$E = \frac{\sum_i E_i v_i}{a^3}; \tag{9}$$

with E = respective quantity, v_i = volume of element i, a = edge length of unit cell. The system of linear Eq. (8) was solved by an in-house software using singular value decomposition SVD.[47] A number of three and six simulations with different loads were required for each structure to determine all λ_{ij} and c_{ij}, respectively.

From the λ_{ij} and c_{ij} the polycrystalline material properties λ, E and ν were estimated according to the Hashin–Shtrikman[4,15] and Voigt–Reuss–Hill[48–50] approximation, respectively. Although those approximations are still widely used, they are considered inaccurate in very anisotropic media.[51] Therefore, an additional simulation of polycrystalline properties was performed: the unit cell was replaced by a single hexahedral element of a homogeneous anisotropic material (SOLID70 and SOLID64 for thermal and mechanical simulations, respectively). Thermal or elastic material properties of the hexahedral elements were set to the values obtained for the respective unit cell. Then a large cube was constructed from $10 \times 10 \times 10$ of such elements where the orientation of the material property tensor within each element has been randomly chosen. The material properties of the large cube were determined by applying loads as described for the small unit cell. Nearly isotropic behaviour was obtained and computation time was less than one minute for this last step of the simulation. All data obtained from this "polycrystal" simulation were within the range of the Hashin–Shtrikman and Voigt–Reuss–Hill approximation, respectively.

2.4. Convergence and verification

Fig. 9 shows the convergence of the FEM results when mesh size was decreased by increasing the number of nodes on the line segments of the model. A sufficient convergence for thermal conductivity, Young's modulus and Poisson's ratio was achieved within 2% with a mesh size corresponding to 6–10 nodes. Note that in Fig. 9 and in the following figures scaled material properties were used, where the respective property of the solid phase corresponds to 100%. The convergence for the stress concentration factor was distinctly worse which was attributed to its local determination in regions showing a very high stress gradient. So in the following sections stress concentration factors should be considered as a rough estimate. Altogether convergence was much better than in simulations with hexahedral elements. Although hexahedral elements are widely used, they were not appropriate to represent the fine structures at the particle contacts in the present study. For spherical particles with very small contacts analytical solutions exist for thermal conductivity[52] and elastic properties.[45,53] Fig. 10 shows a comparison of our FE simulation with the analytical results. (Note that a scaled neck area was used which was calculated by divid-

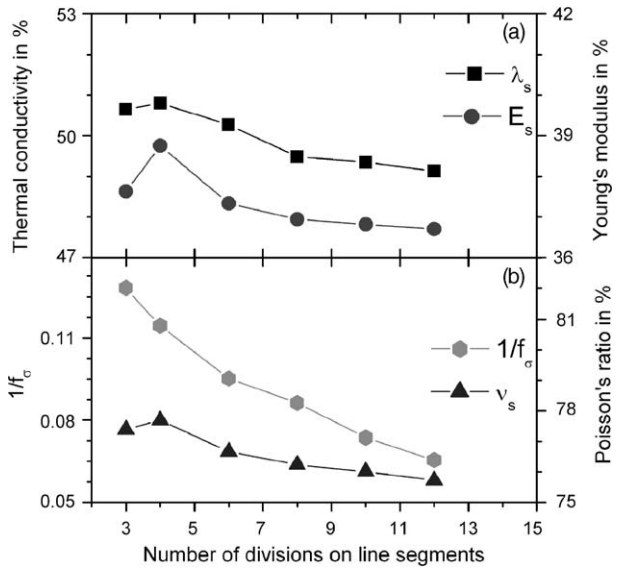

Fig. 9. Convergence of FE simulation determined by variation of material properties with number of nodes on line segments (mesh size) for a simple cubic arrangement of truncated spheres (solid volume fraction 70%): (a) scaled thermal conductivity λ_s and Young's modulus E_s and (b) inverse stress concentration factor $1/f_\sigma$ and scaled Poisson ratio ν_s.

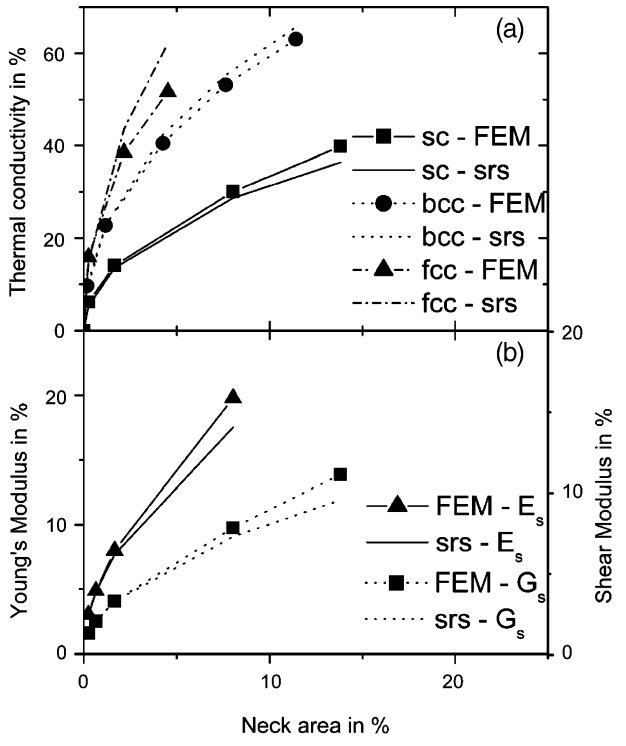

Fig. 10. Comparison of material properties calculated by present FE model and theoretical small radii solutions (srs): (a) scaled thermal conductivities for sc, bcc and fcc structures and (b) scaled Young's and shear moduli for simple cubic arrangement (srs equations from Ref. [45,52,53])

ing the two particle contact area by the side area of the cube.) The excellent agreement demonstrates that the FE model was appropriate for the simulation of structures with very small particle contacts. (Unlike the other figures that show polycrystalline results obtained by the FE method described in the previous paragraph, Fig. 10 shows single crystal material properties in the [1 0 0] direction.)

To avoid handling errors the simulations were performed completely in batch mode. Geometric properties of the model were controlled twice after generating the model in ANSYS and after meshing. If deviations were detected between solid volume fraction, particle contact areas or interface areas to those values determined by the independent computer program, which had generated the structures the simulation was automatically aborted.

3. Results and discussion

Fig. 11 shows the resulting distributions of heat flux and stress in a particle, which had been subjected to a thermal gradient and uniaxial tensile strain, respectively. One can see that flux and stresses are largest in the contact region. Especially large values are observed at the edges of the sintering necks. This was already observed in previous work on heat flow.[26] The concentration of heat flux and mechanical stress at the edges of the particle contacts was observed for various particle shapes and arrangements investigated during the present study. Fig. 12 shows thermal conductivity, Young's modulus, Poisson's ratio and stress concentration factor for different particle shapes. Solid volume fraction was always 70% and the particle arrangement was simple cubic. For comparison also a simple cubic microstructure with 30% of closed spherical pores was presented (Fig. 12) because its 'contact area'—which corresponds to the minimum solid area—was much higher than for the bi-continuous microstructures.

The differences in the thermoelastic properties of particles of very different shapes (compare Figs. 1, 3 and 4) are surprisingly small. Only the Lego brick structure (Fig. 2) shows considerably lower thermal conductivities and Young's moduli than the other particle shapes. Besides this structure, which is rather extreme, the small differences between properties of different shapes and equal contact areas are in good agreement to the minimum solid area approach. However, there are considerable quantitative differences reflected by the convex curvature of the FEM curves in Fig. 12. (The minimum solid area approach would simply yield straight lines through the origin with slope 1.) The reason for the discrepancy is seen in the concentration of heat flux and stress at the edges of the particle contacts (compare Fig. 11). This allows for a larger heat and force transfer—especially with small particle contacts—than it would be expected from a purely geometrical consideration.

The curvature of the Young's modulus data was somewhat smaller than for the thermal conductivity data (Fig. 12a and b). The steeper increase at small particle contacts for thermal

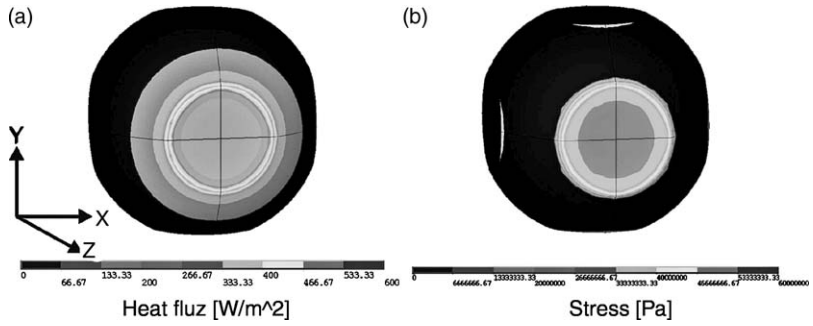

Fig. 11. Contour maps of: (a) heat flux and (b) first principal stress. Temperature gradient and strain were applied in the z-direction.

conductivity corresponded to the larger gradient in heat flux across the particle contact compared to the stress gradient (compare Fig. 11). Considering polycrystals, Poisson's ratio did not go to zero with decreasing contact area (Fig. 12c). For the cube structure with 24 cylindrical contacts it was even nearly independent of contact area. By way of contrast the Poisson's ratios of the respective single crystals in the [1 0 0] direction all approached zero with decreasing neck area (not shown in Fig. 12). Other groups have also suggested a convergence of the Poisson's ratio to finite values with decreasing contact area[13,37] which has been controversially discussed based on different experimental[54] and theoretical results.[55] The stress concentration factor f_σ took very high values at small contact areas, which reflected the inferior strength of porous compacts during the first sintering stage. (Note that $1/f_\sigma$ is shown in the figures to facilitate comparison with the other properties.) The structures with cylindrical contacts (compare Figs. 1c, 2a and 2b) show a distinctly smaller stress concentration at medium contact areas than the other structures. This was attributed to the more homogeneous distribution of stress along the cylindrical contacts compared to the notched contact regions of the other particle shapes. The particle shapes with minimised energy show a steep increase of $1/f_\sigma$ when neck area exceeds 30% (Fig. 12d). This was correlated to a similar increase of the dihedral angle which leads to a smoothing of the particle surfaces in the contact region (compare Fig. 4c).

Fig. 13 shows the effect of particle displacement in a cubic super cell with 64 spherical particles and a solid volume fraction of 70%. A displacement of the particles towards the centre had exactly the same effect as a displacement with the opposite sign reflecting the high symmetry of the transformation used (Eq. (2)), in which the corners and the centre of the unit cell simply changed their role as nucleation centre for agglomerates. Increasing displacement was correlated with a decrease in thermal conductivity, Young's modulus and Poisson's ratio (Fig. 13). This was explained qualitatively by the formation of a matrix of weakly bonded particles in which the 'agglomerates' of more strongly bonded particles were embedded. (It is well known that for inclusions the matrix properties dominate the properties of the composite.[21]) Fig. 13b and c also show various geometric properties of the microstructures. The number of contacts per particle was six for all displacements shown. (It would

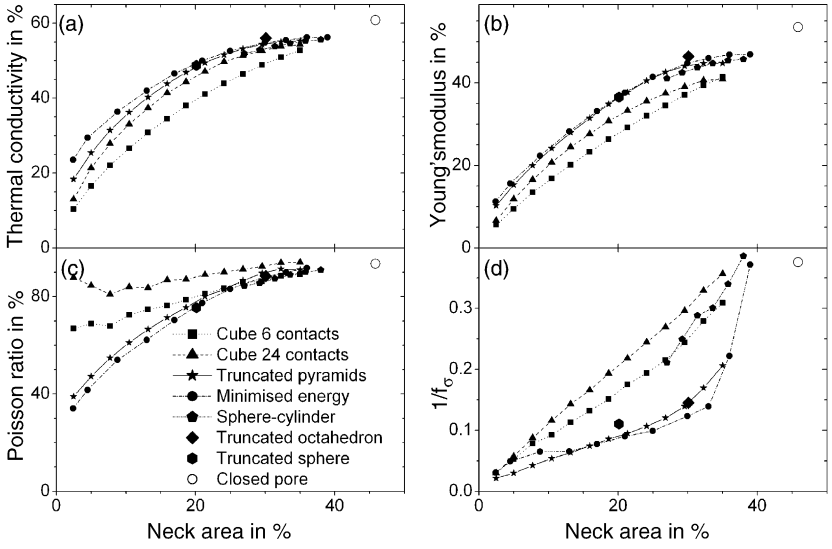

Fig. 12. Material properties at different particle shapes and constant solid volume fraction of 70%: (a) scaled thermal conductivity, (b) scaled Young's modulus, (c) scaled Poisson's ratio, and (d) inverse stress concentration factor.

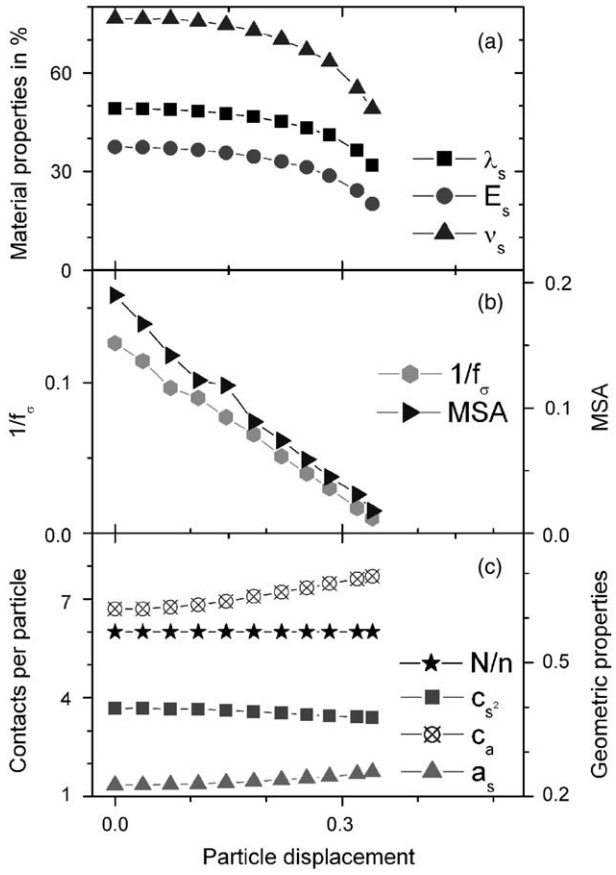

Fig. 13. Properties of cubic structures at different displacements of truncated spherical particles and constant solid volume fraction of 70%: (a) scaled thermal conductivity λ_s, Young's modulus E_s and Poisson ratio ν_s, (b) related inverse stress concentration factor $1/f_\sigma$ and minimum solid area MSA, (c) contacts per particle N/n, average squared solid chord length c_{s^2}, auto-correlation parameter c_a and ratio between total contact area and total pore–solid interface area a_s.

strongly decrease for larger displacements but this would not reflect reasonable structures since the agglomerates would be completely isolated within the pores.) Since the particle contacts within one microstructure had different sizes the scaled neck area could no longer be used as a measure for the geometrical change. Instead the ratio a_s from total contact area and total pore–solid interface area within the unit cell was used. The parameter a_s is dimensionless and independent of the size of the unit cell. It showed a small increase with increasing particle displacement which reflected the non-linear increase of contact area with decreasing centre distance of spherical particles. Also the squared solid chord lengths c_{s^2}, the auto-correlation parameter c_a (compare Eqs. (3) and (4)) and the minimum solid area are shown in Fig. 13. Minimum solid area decreased with increasing displacement and decreasing material properties (Fig. 13b) according to the minimum solid area approach.

Fig. 14 shows the effect of different particle size ratios in the cubic super cell with 64 spherical particles and a solid volume fraction of 70%. The thermoelastic properties for a homogeneous arrangement of large and small particles (compare Fig. 5) versus the particle size ratio are displayed in Fig. 14a and the corresponding geometric parameters in Fig. 14b and c. (The particle size ratio was defined by the ratio of the volumes of a large and a small particle, respectively.) At a size ratio between 1 and 2.5 there was a decrease in the curves of thermal conductivity and Young's modulus. The inverse stress concentration factor showed a pronounced decrease at this size ratio (Fig. 14b). This was correlated to a decrease in the average number of contacts per particle (compare Fig. 14c), caused by vanishing particle contacts between neighbouring particles of the small size category. The high stress concentration at this size ratio was attributed to the smallest particle contacts. Stress concentration decreased after these contacts were released. The results for an inhomogeneous arrangement of large and small particles and the corresponding geometric parameters are shown in Fig. 14d–f. A similar correlation between the material properties and the average number of particle contacts was observed as in the case of homogeneous arrangement. Different from the homogeneous arrangement, an increase in Young's modulus and thermal conductivity was observed for large size ratios (Fig. 14d) with the inhomogeneous arrangement. This was attributed to the load-bearing capability of the spatial structure shown in Fig. 5b, which was enhanced by the volume increase and the corresponding increase of contact area between the large particles at the edges. The increase of Young's modulus was correlated to an increase in the squared solid chord lengths c_{s^2}, which was considered reasonable since c_{s^2} was introduced as a measure for the length of force transmission that was very large at the edges of the unit cell. There was a close correlation between thermal conductivity and Young's modulus (Fig. 14a and d). Correlation between minimum solid area and material properties was poor—especially in the homogeneous particle arrangement (Fig. 14a and b).

The effect of particles coordination on thermoelastic properties is shown in Fig. 15. The symmetry of the unit cell was varied from sc to bcc and fcc for a fixed volume fraction of solid phase of 80% (Fig. 15a). Additionally the same structures were calculated for a fixed area ratio a_s of 0.1 corresponding to a solid volume fraction f_s of 61.5, 76.7 and 80.1% for the sc, bcc and fcc structures, respectively (Fig. 15d). The geometric parameters to these structures are shown in Fig. 15b, c, e and f. Thermoelastic properties decreased when coordination number was increased with constant solid volume fraction (Fig. 15a). This could be explained by the previous results considering the area ratio a_s of these structures, which was drastically decreased by 80% when the coordination number was increased from 6 to 12 (Fig. 15c). When the coordination number was increased at the same level of a_s the thermoelastic properties increased (Fig. 15d). Also the stress concentration factor decreased which demonstrated that stress was distributed more homogeneously in the microstructures with more particle contacts. Whereas the increase in coordination number was related to an increase

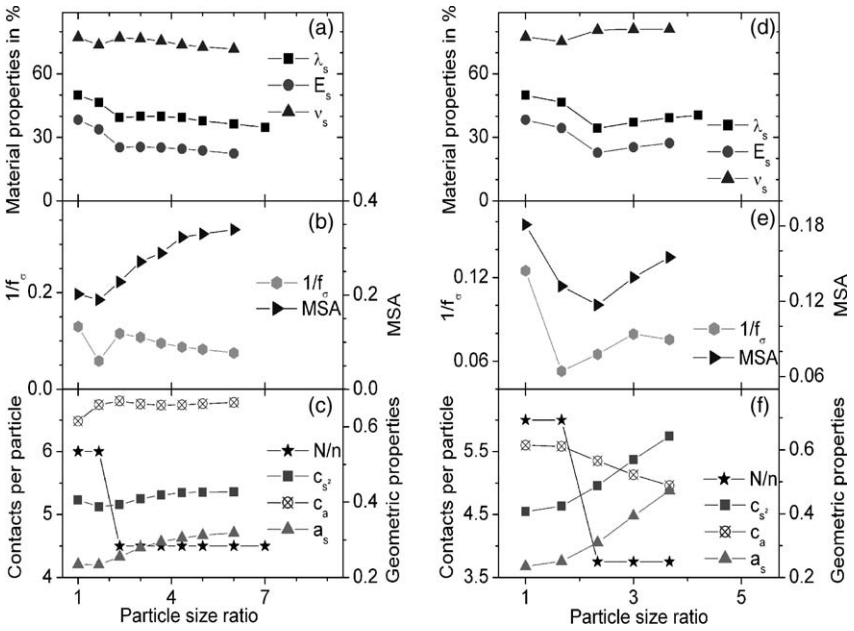

Fig. 14. Properties of cubic structures at different size ratios of truncated spherical particles and constant solid volume fraction of 70%: (a) scaled thermal conductivity λ_s, Young's modulus E_s and Poisson ratio ν_s, for particles arranged homogeneously, (b) related inverse stress concentration factor $1/f_\sigma$ and minimum solid area MSA and (c) related contacts per particle N/n, average squared solid chord length c_{s^2}, auto-correlation parameter c_a and ratio between total contact area and total pore–solid interface area a_s, (d) material properties for particles arranged inhomogeneously, (e) related inverse stress concentration factor and minimum solid area and (f) related geometric properties.

in the auto-correlation parameter for constant volume fractions (Fig. 15a and c), with constant area ratio this increase was related to an increase in the squared solid chord lengths (Fig. 15d and f). As in Fig. 14 correlation between minimum solid area and material properties was poor—especially with fixed solid volume fraction f_s (Fig. 15a and b).

Fig. 16 shows a summary of results obtained for random arrangements of spheres. In all cases the solid volume fraction

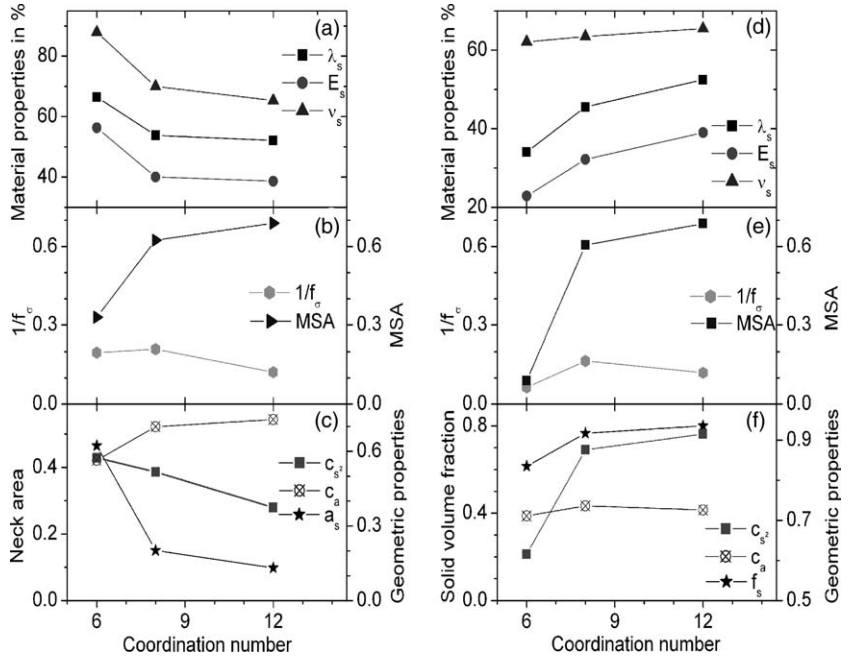

Fig. 15. Material properties of cubic structures at different number of nearest neighbours: (a) scaled thermal conductivity λ_s, Young's modulus E_s and Poisson ratio ν_s, for particles with constant solid volume fraction of 80%, (b) related inverse stress concentration factor $1/f_\sigma$ and minimum solid area MSA and (c) related contacts per particle N/n, average squared solid chord length c_{s^2}, auto-correlation parameter c_a and ratio between total contact area and total pore–solid interface area a_s, (d) material properties for particles with constant scaled contact area $a_s = 0.1$ at different solid volume fractions f_s, (e) related inverse stress concentration factor and minimum solid area and (f) related geometric properties.

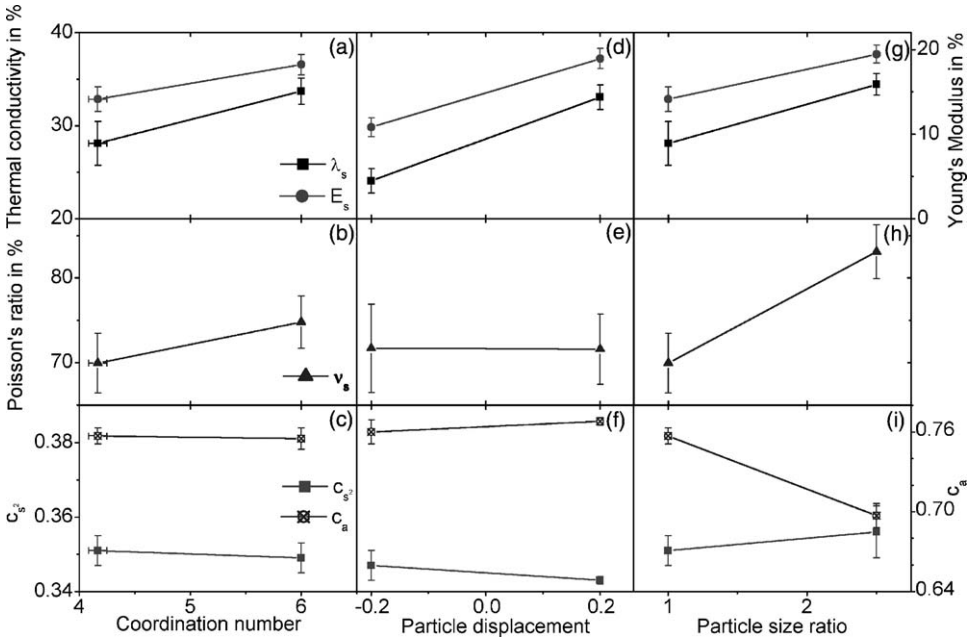

Fig. 16. Material properties at random arrangements of truncated spheres (solid volume fraction 70% and scaled contact area $a_s = 0.1$): (a) scaled thermal conductivity λ_s and Young's modulus E_s, (b) scaled Poisson's ratio ν_s, (c) average squared solid chord length c_{s^2} and auto-correlation parameter c_a for different coordination numbers, (d–f) corresponding quantities for different particle displacements, and (g–i) corresponding quantities for different particle size ratios.

f_s was 70% and the area ratio a_s was 0.1, but coordination number, particle displacement and particle size ratio were changed (Fig. 16a–c, respectively). Each point in Fig. 16 was the mean value of 10 independent runs for different random structures obtained with equal boundary conditions. (Note that the error bars in Fig. 16 indicate uncertainty derived from statistical spread of results from different simulation runs and not measuring errors.) Thermoelastic properties increased with increasing coordination number (Fig. 16a and b), which corresponds to the cubic lattices if the area ratio was fixed (compare Fig. 15d). A particle displacement to the centre of the unit cell caused an increase and an outward displacement a decrease of thermal conductivity and Young's modulus (Fig. 16d). This was attributed to a more efficient formation of a load-bearing frame by concentrating the spheres in the centre compared to the less dense distribution on the surfaces of the unit cell. An increase of material properties was also observed with increasing particle size ratio (Fig. 16g and h). This was explained by the improvement of force and heat transmission within the large spheres, which lead to higher stresses and temperature gradients at the particle contacts. Minimum area was not determined for the random structures. Since it could not be expected that several particle contacts were in the same plane the minimum solid area concept was considered applicable only after some modification. The other geometric properties which were calculated from chord length analysis did not show a clear correlation to the thermoelastic properties.

4. Conclusions

Particle shapes which allow for an independent variation of contact area and solid volume fraction (compare Figs. 2–4) offer much larger flexibility in the modelling of microstructures than the widely used truncated spheres. For this reason additional particle shapes and arrangements were used to simulate bi-continuous structures, which occur in porous ceramics. It was shown that phenomena related to particle arrangement could be simulated in cubic super cells. These model structures were not proposed to get an accurate imaging of real structures, but to understand the effects, which contribute to microstructure property relations. Many more cubic model structures are possible than were used in the present paper. They have to be constructed by some abstraction from the real structures, which can readily be done.

Random structures have the advantage to reproduce the disorder of real structures. It has been shown that they offer more flexibility to control simultaneously geometric parameters like solid volume fraction, contact area and coordination number than cubic structures. This makes them more appropriate to investigate the influence of one microstructure parameter without unwillingly changing other parameters. However, the use of random structures without such control is at a disadvantage compared to cubic structures since interpretation of results will be difficult. A disadvantage of the random microstructures was the computational effort, which was two to three orders of magnitudes larger than the effort for an accurate simulation of cubic structures.

Thermal conductivity and Young's modulus were closely correlated in all porous compacts investigated in the present study. Parameters like coordination number, particle size distribution and shape, agglomeration, pore volume and contact area affected both properties similarly. The largest changes were caused by the contact area between the particles. Therefore, in comparing porous ceramics with different microstructures thermal conductivity as well as Young's modulus are a good measure for changes in contact area. Together with the measurement of total pore volume they can provide a valuable complement to ceramographic methods. Although the Young's modulus showed the same trend as the thermal conductivity, the scaled Young's moduli were always smaller by 20–50% than the respective scaled thermal conductivity data. This was attributed to the larger capability of heat flux to bypass thermal barriers compared to force transmission, which is most efficient along straight lines. Microstructure parameters which were determined in the present study by chord length and minimum solid area analysis, i.e. squared chord lengths, auto-correlation etc., did not show unambiguous correlation to the changes of thermoelastic properties. Some of the phenomena could be correlated to a specific parameter, but the unambiguous interpretation was obscured by other parameters, e.g. number of particle contacts and size distribution, which cannot be derived from image analysis of polished sections with real materials. Considering the large effort of sample preparation and image analysis to achieve these parameters it is proposed to utilise measurements of material properties for the investigation of microstructure phenomena. The advantages of this inverse procedure are enhanced by the opportunity to obtain thermoelastic properties by in situ measurements during sintering of ceramic materials.[40,56]

Stress concentration in porous ceramics strongly depends on particle shape (compare Fig. 12). It can be decreased by smoothing the notches at the particle contacts. This can be realised by increasing the dihedral angle and by using small particle bridges between larger particles or particle clusters. An example of the use of the simulation could be the design of porous ceramics with high thermal shock resistance. For most ceramic samples the Biot number β is very small. Then thermal shock resistance $\Delta T/t$ is proportional to[57]:

$$\frac{\Delta T}{t} \propto \frac{\sigma(1-\nu)}{E\alpha\beta};\quad \beta = \frac{rh}{\lambda};\quad \sigma \propto \frac{1}{f_\sigma} \Rightarrow \frac{\Delta T}{t} \propto C\frac{(1-\nu)\lambda}{f_\sigma E}; \tag{10}$$

with σ = strength, α = coefficient of thermal expansion, r = characteristic length of heat transfer, h = surface heat transfer coefficient and C = constant including those parameters which only weakly depend on microstructure. Using the right part of Eq. (10), thermal shock resistance was estimated from the thermal conductivity λ, Young's modulus E, Poisson's ratio ν and inverse stress concentration factor $1/f_\sigma$ shown in Fig. 12 (Fig. 17). (Thereby it was assumed that strength σ was proportional to $1/f_\sigma$ which requires that critical flaws do not interfere with microstructure changes.) Thermal shock resistance for the Lego brick like particles shown in Fig. 2 was much higher than that for the truncated pyramid particles shown in Fig. 3. Assuming that there are no other effects reducing the strength, a very large influence of particle shape on thermal shock resistance was predicted. If the pore phase is replaced by another solid phase, additional stresses arise due to mismatch in thermal expansion. Those binary composites were already simulated using the same model as the one used in the present study. Strength was significantly affected by thermal stresses.[58]

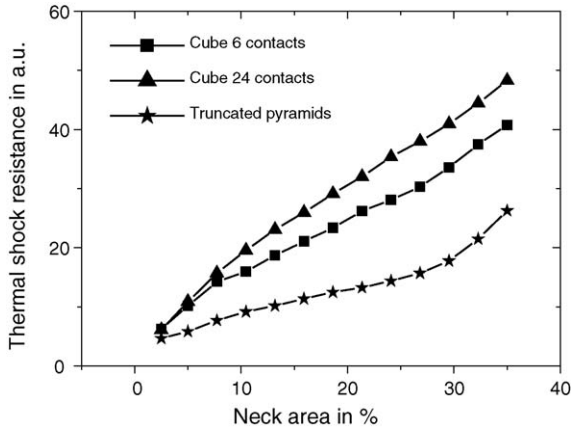

Fig. 17. Scaled thermal shock resistance estimated for simple cubic structures and different particle shapes at a solid volume fraction of 70%: cube with 6 cylindrical contacts, cube with 24 cylindrical contacts, enclosed cube with 6 truncated square pyramids.

Although the present results are considered helpful in understanding some basic relations between microstructure phenomena and material properties, the formation of the microstructures was not considered yet. Future work will concentrate on the effect of diffusion on neck geometry and the investigation of more realistic microstructures.

Acknowledgements

The authors acknowledge the help of N. Siedow, D. Kuhnke[59] from ITWM Kaiserslautern for the verification of some of the models and Fraunhofer Gesellschaft for financial support within the joint project "multiscale modelling".

References

1. Hashin, Z. and Shtrikman, S., On some variational principles in anisotropic and nonhomogeneous elasticity. *J. Mech. Phys. Solids*, 1962, **10**, 335–342.
2. Nye, J. F., *Physical Properties of Crystals*. University Press, Oxford, 1957.
3. Boccaccini, A. R. and Fan, Z., A new approach for the Young's modulus-porosity correlation of ceramic materials. *Ceram. Int.*, 1997, **23**, 239–245.

4. Hale, D. K., The physical properties and composite materials. *J. Mater. Sci.*, 1976, **11**, 2105–2141.
5. Hill, R., Elastic properties of reinforced solids: some theoretical principles. *J. Mech. Phys. Solids*, 1963, **11**, 357–372.
6. Jefferson, G., Haritos, G. K. and McMeeking, R. M., The elastic response of a cohesive aggregate—a discrete element model with coupled particle interaction. *J. Mech. Phys. Solids*, 2002, **50**, 2539–2575.
7. Kovàcik, J., Correlation between shear modulus and porosity in porous materials. *J. Mater. Sci. Lett.*, 2001, **20**, 1953–1955.
8. Martin, R. B. and Haynes, R. R., Confirmation of theoretical relation between stiffness and porosity in ceramics. *J. Am. Ceram. Soc.*, 1971, **54**, 410–411.
9. Mukhopadhyay, A. K. and Phani, K. K., Young's modulus-porosity relations: an analysis based on a minimum contact area model. *J. Mater. Sci.*, 1998, **33**, 69–72.
10. Munro, R. G., Effective medium theory of the porosity dependence of bulk moduli. *J. Am. Ceram. Soc.*, 2001, **84**, 1190–1192.
11. Pabst, W. and Gregorová, E., Derivation of the simplest exponential and power-law relations for the effective tensile modulus of porous ceramics via functional equations. *J. Mater. Sci. Lett.*, 2003, **22**, 1673–1675.
12. Pettermann, H. E., Böhm, J. H. and Alcalá, J., Normalized diagrams for micromechanical estimates of the elastic response of composite materials. *Metall. Mater. Trans. A*, 2002, **33a**, 3187–3199.
13. Ramakrishnan, N. and Arunachalam, V. S., Effective elastic moduli of porous ceramic materials. *J. Am. Ceram. Soc.*, 1993, **76**(11), 2745–2752.
14. Sudduth, R. D., A generalized model to predict the effect of voids on modulus in ceramics. *J. Mater. Sci.*, 1995, **30**, 4451–4462.
15. Hashin, Z. and Shtrikman, S., A variational approach to the theory of the elastic behaviour of multiphase materials. *J. Mech. Phys. Solids*, 1963, **11**, 127–140.
16. Boccaccini, A. R., Ondracek, G., Mazilu, P. and Windelberg, D., On the effective Young's modulus of elasticity for porous materials: microstructure modelling and comparison between calculation and experimental values. *J. Mech. Behav. Mater.*, 1993, **2**, 119–128.
17. Chu, Y. C. and Rokhlin, S. I., Effective elastic moduli of fiber-matrix interphases in high-temperature composites. *Metall. Mater. Trans.*, 1996, **27a**, 165–182.
18. Dean, E. A., Elastic moduli of porous sintered materials as modelled by a variable-aspect-ratio-self-consistent oblate-spheroidal-inclusion theory. *J. Am. Ceram. Soc.*, 1983, **12**, 847–855.
19. Jeong, H. and Hsu, D. K., Quantitative estimation of material properties of porous ceramics by means of composite micromechanics and ultrasonic velocity. *NDT & E Int.*, 1996, **2**, 95–101.
20. Miloh, T. and Beneviste, Y., A generalized self-consistent method for the effective conductivity of composites with ellipsoidal inclusions and cracked bodies. *J. Appl. Phys.*, 1988, **63**, 789–796.
21. Ondracek, G., Zur Leitfähigkeit von mehrphasigen Werkstoffen—Vergleich zwischen experimentellen und berechneten Werten von Cermets. *Z. f. Werkstofftechnik/J. Mater. Technol.*, 1974, **5**, 416–428.
22. Rice, R. W., Relation of tensile strength-porosity effects in ceramics to porosity dependence of Young's modulus and fracture energy, porosity character and grain size. *Mater. Sci. Eng.*, 1989, **A112**, 215–224.
23. Rice, R. W., Evaluation and extension of physical property—porosity models based on minimum solid area. *J. Mater. Sci.*, 1996, **31**, 102–118.
24. Tobochnik, J., Laing, D. and Wilson, G., Random-walk calculation of conductivity in continuum percolation. *Phys. Rev. A*, 1990, **41**, 3052–3058.
25. Raether, F. and Müller, G., Novel characterization of process and product for AlN ceramics and correlation with thermal conductivity. In *Proceedings of the International Symposium on Aluminium Nitride Ceramics*, 1998.
26. Hahn, O., *Models for the heat transport in sintering ceramic powder compacts*, Ph.D. thesis, University of Würzburg, Germany, 1996.
27. Birnboim, A., Olorunyolemi, T. and Carmel, Y., Calculating the thermal conductivity of heated powder compacts. *J. Am. Ceram. Soc.*, 2001, **84**, 1315–1320.
28. Pistor, C. M., Yardimci, M. A., Jasiak, K. J. and Güceri, S. I., Thermal conductivity of composite materials. In *Proceedings of the 28th International SAMPE Technical Conference*, 1996, pp. 564–573.
29. Sheikh, M. A., Taylor, S. C., Hayhurst, D. R. and Taylor, R., Microstructural finite-element modelling of a ceramic matrix composite to predict experimental measurements of its macro thermal properties. *Model. Simul. Mater. Sci. Eng.*, 2001, **9**, 7–23.
30. Biswas, R., Hanshall, J. L. and Wakeman, R. J., Finite-element modeling of elastic stress distributions in composite materials. *Mech. Compos. Mater. Struct.*, 1997, **4**, 233–249.
31. Goussev, O. A., Richner, P., Rozman, M. G. and Gusev, A. A., Void-containing materials with tailored Poisson's ratio. *J. Appl. Phys.*, 2000, **7**, 4013–4016.
32. Gusev, A. A., Hine, P. J. and Ward, I. M., Fiber packing and elastic properties of a transversely random unidirectional glass/epoxy composite. *Compos. Sci. Technol.*, 2000, **60**, 535–541.
33. Gusev, A. A. and Lusti, R. H., Rational design of nanocomposites for barrier applications. *Adv. Mater.*, 2001, **21**, 1641–1643.
34. Kartuzov, V. V., Rotmistrovskii, K. E., Stepanenko, A. V. and Trefilov, V. I., A method of predicting the elastic characteristics of diamond composites. *Powder Metall. Metal Ceram.*, 2001, **40**(11–12), 612–617.
35. Öchsner, A., *Experimentelle und numerische Unersuchung des elastoplastischen Verhaltens zellularer Modellwerkstoffe, Fortschritt-Berichte VDI* (Reihe 18, Nr. 282). VDI Verlag, Düsseldorf, 2003.
36. Park, J. S. and Sun, C. T., Micromechanical modelling of co-continuous ceramic metal composites. In *Proceedings of the American Society of Composites, 16th Technical Conference*, 2001, pp. 123–134.
37. Roberts, A. P. and Garboczi, E. J., Elastic properties of model porous ceramics. *J. Am. Ceram. Soc.*, 2000, **83**, 3041–3048.
38. Roberts, A. P. and Garboczi, E. J., Elastic properties of model random three-dimensional open-cell solids. *J. Mech. Phys. Solids*, 2002, **50**, 33–55.
39. Scherer, G. W., Calas, S. and Sempéré, R., Densification kinetics and structural evolution during sintering of silica aerogel. *J. Non-Cryst. Solids*, 1998, **240**, 118–130.
40. Raether, F. and Springer, R., In-Situ measurement of neck formation during sintering of alumina by a novel thermooptical measuring device. *Adv. Eng. Mater.*, 2000, **2**, 741–744.
41. Hardy, D. and Green, J., Mechanical properties of a partially sintered alumina. *J. Eur. Ceram. Soc.*, 1995, **15**, 769–775.
42. Dorey, R. A., Yeomans, J. A. and Smith, P. A., Effect of pore clustering on the mechanical properties of ceramics. *J. Am. Ceram. Soc.*, 2002, **22**, 403–409.
43. Brakke, K., The surface evolver. *Exp. Math.*, 1992, **1**, 141–165.
44. German, R. M., *Sintering Theory and Practice*. John Wiley & Sons, New York, 1996.
45. Walton, K., The effective elastic moduli of a random packing of spheres. *J. Mech. Phys. Solids*, 1987, **32**(2), 213–226.
46. Exner, H. E. and Hougardy, H. P., ed., *Quantitative Image Analysis of Microstructures*. DGM Informationsgesellschaft Verlag, 1988.
47. Press, W. H., Flannery, B. P., Teukolsky, S. A. and Vetterling, W. T., *Numerical Recipes*. Cambridge University Press, Cambridge, 1989.
48. Voigt, W., *Lehrbuch der Kristallphysik*. Teubner, Leipzig, 1928.
49. Reuss, A., Berechnung der Fließgrenze von Mischkristallen auf Grund der Plastizitätsbedingung für Einkristalle. *ZAMM*, 1929, **9**, 49–58.
50. Den Toondert, J. M. J., van Dommelen, J. A. W. and Baaijens, F. P. T., The relation between single crystal elasticity and the effective elastic behaviour of polycrystalline materials: theory, measurement and computation. *Model. Simul. Mater. Sci. Eng.*, 1999, **7**, 909–928.
51. Kumar, S. and Singh, R. N., Thermal conductivity of polycrystalline materials. *J. Am. Ceram. Soc.*, 1995, **78**, 728–736.
52. Kaviany, M., *Principles of Heat Transfer in Porous Media Mechanical Engineering Series*. Springer-Verlag, 1991.

53. Walton, K., The effective elastic moduli of model sediments. *Geophys. J. R. Astr. Soc.*, 1975, **43**, 293–306.
54. Boccacini, A. R., Comment on "Effective elastic moduli of porous ceramic materials". *J. Am. Ceram. Soc.*, 1994, **77**(10), 2779–2781.
55. Rice, R. W., Comment on "Effective elastic moduli of porous ceramic materials". *J. Am. Ceram. Soc.*, 1995, **78**(6), 1711.
56. Stanullo, J., Lyamshev, M. L. and Busse, G., Thermoacoustic vibrometry for in-situ monitoring of processes. *Mater. Sci. Forum*, 1996, **210–213**, 303–308.
57. Collin, M. and Rowcliffe, D., Analysis and prediction of thermal shock in brittle materials. *Acta Mater.*, 2000, **48**, 1655–1665.
58. Raether, F., Durschang, B., Thiel, N., Microstructural design of a CAD/CAM machinable infiltration ceramic with high strength and near net shape performance, *Material Week 2002*, *Symp. M*, *Ceramics*. Munich, Germany, 2002. Available from: www.materialsweek.org.
59. Kuhnke, D., *Homogenization of the Heat Conduction in Ceramic Materials*. Diploma thesis, University of Kaiserslautern, 2000.
60. Beere, W., A unifying theory of the stability of penetrating liquid phases and sintering pores. *Acta Metalurgica*, 1975, **23**, 131–138.